

pubs.acs.org/JPCC Article

Examining the Influence of Bilayer Structure on Energy Transfer and Molecular Photon Upconversion in Metal Ion Linked Multilayers

Published as part of The Journal of Physical Chemistry virtual special issue "Josef Michl Festschrift".

Ashley Arcidiacono, Yan Zhou, Wendi Zhang, Jeffrey O. Ellison, Suliman Ayad, Erica S. Knorr, Autumn N. Peters, Lianqing Zheng, Wei Yang, S. Scott Saavedra, and Kenneth Hanson.



Cite This: J. Phys. Chem. C 2020, 124, 23597-23610



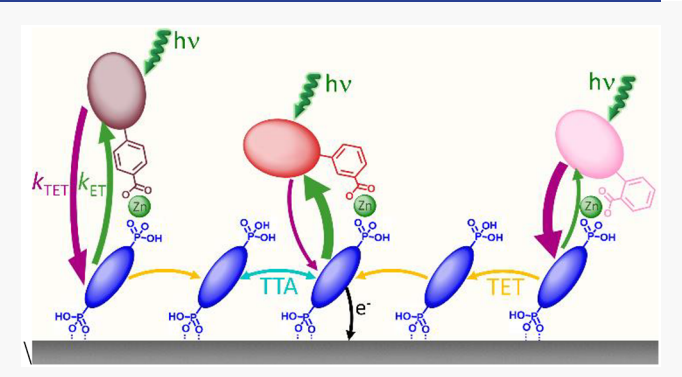
ACCESS

III Metrics & More

Article Recommendations

s Supporting Information

ABSTRACT: Metal ion linked multilayers are a unique motif to spatially control and geometrically restrict molecules on a metal oxide surface, which is of interest in a number of promising applications. Here we use a bilayer composed of a metal oxide surface, an anthracene annihilator molecule, Zn(II) linking ion, and porphyrin sensitizers to probe the influence of the position of the metal ion binding site on energy transfer, photon upconversion, and photocurrent generation. Despite being energetically similar, varying the position of the carboxy metal ion binding group (i.e., ortho, meta, para) of the Pt(II) tetraphenyl porphyrin sensitizer had a large impact on energy transfer rates and upconverted photocurrent that can be attributed to differences in their geometries. From polarized attenuated total reflectance



measurements of the bilayers on ITO, we found that the orientation of the first layer (anthracene) was largely unperturbed by subsequent layers. However, the tilt angle of the porphyrin plane varies dramatically from 41° to 64° to 57° for the p-, m-, and o-COOH substituted porphyrin molecules, which is likely responsible for the variation in energy transfer rates. We go on to show using molecular dynamics simulations that there is considerable flexibility in porphyrin orientation, indicating that an average structure is insufficient to predict the ensemble behavior. Instead, even a small subset of the population with highly favorable energy transfer rates can be the primary driver in increasing the likelihood of energy transfer. Gaining control of the orientation and its distribution will be a critical step in maximizing the potential of the metal ion linked structures.

1. INTRODUCTION

Molecular photon upconversion via triplet—triplet annihilation (TTA-UC) is of interest for a number of applications including bioimaging, photocatalysis, photodynamic therapy, lighting, solar energy conversion, and more. TTA-UC is typically achieved using a sensitizer and annihilator pair where low energy light is absorbed by the sensitizer and then transferred to the annihilator molecule. When two annihilator molecules in the triplet excited state are in proximity, they can then undergo TTA to generate a higher energy excited state which relaxes via radiative or nonradiative decay pathways.

An overwhelming majority of the TTA-UC research to date has been conducted with sensitizer and annihilator molecules suspended in solution or a rubbery polymer matrix. 6-10 This work has provided unprecedented insights into the mechanism, dynamics, and energetic requirements for realizing efficient TTA-UC. More recently, there has been an increased interest in using structurally restricted motifs like self-assembly, 10,11 lipid membranes, 12 annihilator/sensitizer containing polymers and dendrimers, 13,14 host—guest complexes, 15 ionic crystals, 16

and MOFs^{17,18} in an effort to increase energy transfer rates and ultimately improve TTA-UC efficiencies.

Work in our groups has focused on metal ion linked multilayers on mesoporous metal oxide surfaces (Figure 1a) 19,20 as a structured motif to not only facilitate TTA-UC but also directly extract charge from the upconverted state. The latter is important for enabling integrated TTA-UC solar cells that have the potential to surpass the Shockley–Queisser limit (\sim 33%).

Photocurrent contributions from TTA-UC of up to 0.315 mAcm⁻² have been achieved under ambient 1 sun irradiance (AM1.5),²⁹ which is above the device relevance threshold

Received: September 24, 2020 Revised: September 30, 2020 Published: October 14, 2020





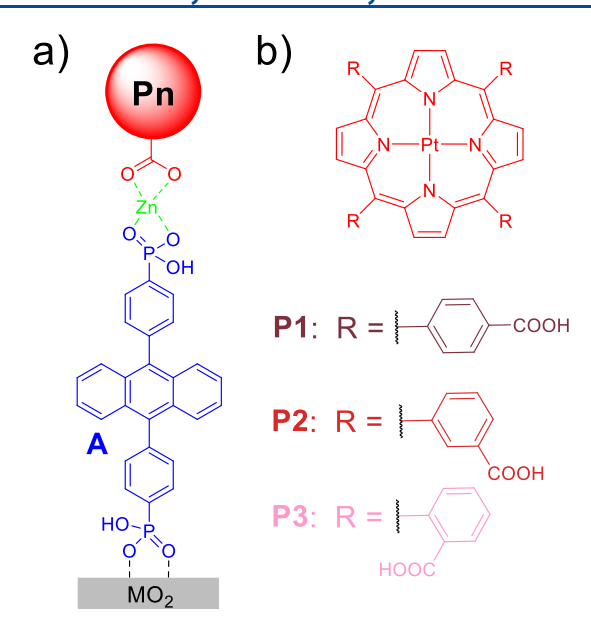


Figure 1. (a) Schematic depiction of the metal ion linked bilayer on a metal oxide surface (MO_2) . (b) Structure of sensitizer molecules P1–P3.

proposed by Schmidt and co-workers.³⁰ However, there is still much room for improvement.²³

Unlike in a solvent or host matrix, where molecules are free to rotate and collide in random orientations, the geometrically fixed nature of the multilayer assembly amplifies the impact of molecular structure and orientation on energy transfer and TTA events. For example, Zhou et al. reported a two-orders of magnitude difference in cross-surface triplet exciton diffusion rates in self-assembled bilayers composed of two energetically similar annihilator molecules with different surface binding position and, presumably, orientations.^{31,32}

Likewise, although many different sensitizers are available (e.g., transition metal complexes, organics, quantum dots, etc.)^{33–35} and even multisenstizer schemes demonstrated,^{29,36,37} insights into the role of sensitizer structure, particularly in structurally restricted TTA-UC schemes, are absent.

Here, we report our investigation into how variations in the position of the metal ion binding group on the sensitizer influences the structure and photophysical properties of the metal ion linked multilayer. The platinum porphyrin sensitizers are shown in Figure 1b and have either para (P1), meta (P2), or ortho (P3) substitution of the carboxylate groups on the meso-phenyl rings. We use a combination of theoretical, spectroscopic, and spectroelectrochemical measurements to gain insights into the structure, energy transfer dynamics, TTA-UC, and solar energy conversion of the bilayer films. As anticipated, variations in the location of the metal ion binding group influences the orientation of the sensitizer and consequently the properties and performance of the films.

2. EXPERIMENTAL SECTION

2.1. Materials. Calcium hydride, potassium hydroxide, boron trifluoride diethyl etherate, anhydrous benzonitrile, dichloromethane, chloroform, ethanol, tetrahydrofuran, and acetone (Sigma-Aldrich), methyl 2-formylbenzenecarboxylate and methyl 3-formylbenzoate (Matrix Scientific), 2.3-dichloro-5,6-dicyano-p-benzoquinone (DDQ) (Alpha Aesar), and P1 (Frontier Scientific) were purchased from the supplier in parentheses and used without further purification. Pyrrole was obtained from Sigma-Aldrich and distilled over calcium hydride prior to use. Common oxygen free Schlenk techniques were used during reactions unless otherwise specified. Fluorine-doped tin oxide (FTO) coated glass (sheet resistance 15 Ω \square ⁻¹) and nonconductive glass were purchased from Hartford Glass Co. Meltonix film (1170-25) and Vac'n Fill syringSe (65209) were purchased from Solaronix. Micro glass cover slides (18 × 18 mm) were obtained from VWR. 4,4'-(Anthracene-9,10-diyl)bis(4,1-phenylene)diphosphonic acid (A in Figure 1)²² and triphenyl-4,4'-diphosphonic acid (B)³⁸ as well as sol-gel pastes for TiO₂ and ZrO₂³⁹⁻⁴¹ prepared following previously published procedures.

2.2. Synthesis. The unmetalated porphyrins for $P2^{42}$ and $P3^{43}$ were synthesized following previously published procedures followed by platination using the traditional $PtCl_2$ in benzonitrile procedure. Synthetic details for P2 and P3 are provided in the Supporting Information. H NMR spectra were recorded on a Bruker 400 MHz FT NMR (Model: Avance-DPX 600) and the spectral shifts are calibrated with respect to residual protonated solvent peaks (δ 7.26 and 2.49 for chloroform- d_6 and dmso- d_6 , respectively). Due to low solubility, we were unable to obtain ^{13}C NMR for the compounds.

2.3. Spectroscopic and Electrochemical Cell Preparation. Photovoltaic cells were prepared similarly to our previously published procedure with details provided in the Supporting Information. ^{21,22}

2.4. Dye Loading. The metal oxide films (MO₂ = TiO₂ or ZrO₂) on FTO glass were functionalized with monolayers of **A** or **B** by soaking in their respective loading solutions (200 μ M **A** in DMSO, 400 μ M **B** in DMSO) for 48 h. The films were then soaked in a solution of Zn(CH₃COO)₂ in MeOH (400 μ M) for 2 h, followed by 200 μ M **P1**–**P3** solution of DMSO for 2 h with N₂ bubbling, resulting in MO₂-A/B-Zn-P1–P3. In accord with the previously published procedure, 46 surface coverages (Γ in mol cm⁻²) are estimated with the expression Γ = $(A(\lambda)/\varepsilon(\lambda))/1000$ where ε is the molar extinction coefficient of **A** (1.27 × 10⁴ M⁻¹ cm⁻¹ at 376 nm)²² and **P1**–**P3** (Table 1) in DMSO²² and $A(\lambda)$ is the absorbance of the film at wavelength λ .

2.5. Spectroscopic Measurements. Details for the absorption, steady-state emission, time-resolved emission, quantum yield, transient absorption, and intensity dependent measurements are provided in the Supporting Information.

Table 1. Photophysical Properties of P1-P3 in N2-Deaerated DMSO

	$\lambda_{\rm abs}$ (nm) (ε , $\times 10^4$ M ⁻¹ cm ⁻¹)	$\lambda_{\rm em} ({\rm nm})^a$	$\tau (\mu s)^{a,b}$	Φ	$k_{\rm r} ({\rm s}^{-1})^c$	$k_{\rm nr} (s^{-1})^d$
P1	404 (25.7), 510 (2.7)	665	9.2	0.007	761	1.08×10^{5}
P2	404 (19.5), 510 (1.9)	665	9.1	0.007	769	1.09×10^{5}
Р3	409 (14.1), 515 (1.5)	685	9.3	0.008	860	1.06×10^{5}

 $^a\lambda_{\rm ex}=410~{\rm nm.}^b$ From an exponential fit to the excited state decay at emission peak value. $^ck_{\rm r}=\Phi/\tau. ^dk_{\rm nr}=(1-\Phi_{\rm FI})/\tau.$

2.6. Photovoltaic Measurements. Photovoltaic measurements were acquired following our previously published procedure with the details provided in the Supporting Information. ^{21,32}

2.7. Attenuated Total Reflectance (ATR). ATR spectroscopy measurements were performed using a custom-built instrument described in previous publications. ^{47,48} Briefly, ITO-coated glass slides (Thin Film Devices) were utilized as planar waveguides. A collimated, polarized broadband source (a Xe lamp) was coupled into and out of the waveguide using two BK7 (n = 1.51) prisms. The two prisms were separated by 42 mm which provided eight total internal reflections at the ITO/solution interface. The internal reflection angle was 68°. The outcoupled light from the waveguide was directed into a monochromator (Newport MS260i) and was detected by a CCD (Andor iDus420A).

A liquid flow cell was used to exchange solutions in contact with the ITO surface. Adsorption isotherms of A binding to ITO and porphyrins binding to A-Zn on ITO were measured using transverse magnetic (TM) polarized light and are shown in the Supporting Information. The adsorption isotherms were used to establish conditions for preparing films for molecular orientation measurements. These conditions are given in Supporting Information (Table S1). Estimates of the surface coverage of A in monolayer films and porphyrins in bilayer films (A-Zn-P1, A-Zn-P2, and A-Zn-P3) are given in the Supporting Information (Table S2).

The mean tilt angles of the absorbance dipoles of A in monolayer films and A and porphyrins in bilayer films were measured using polarized ATR spectroscopy. Sample spectra of these films are presented in the Supporting Information (Figures S1-S6). The method described by Mendes et al. was used to correct for the unequal intensities of the interfacial electric fields in transverse electric (TE) and TM polarizations.⁴⁹ In this method, an adsorbed film of chromophores with a random molecular orientation with respect to the ITO surface is used to normalize the electric field intensity differences. Dextrans labeled with chromophores that adsorb in the same spectral region as the molecule of interest served this purpose. Rhodamine-B dextran films were used in the orientation measurements on P1, P2, and P3 films, and Cascade Blue dextran films were employed in the orientation measurements on A; sample spectra of these films are presented in the Supporting Information. The wavelength ranges for the integration of the A, porphyrin, Rhodamine-B, and Cascade Blue spectra are given in the Supporting Information (Table S1).

2.8. Molecular Dynamics Simulation and Analysis. Structural Model Building. To build the atomistic model for the molecular dynamics (MD) simulation study, as the first step, a multilayer TiO₂ assembly was constructed with 2240 unit cells (4 Ti and 8 O atoms in each unit cell) that leads to a dimension of 91.8 Å \times 99.18 Å \times 33.3 Å. In the assembly bulk, each Ti is 6-coordinated and each O is 3-coordinated. At the surface, each Ti is either 4 or 5-coordinated and each O is 2coordinated. 50 Atoms on the edges along x and y directions are also bonded due to the periodic boundary treatment. The assembly model has only two surfaces (top and bottom), which are in parallel with the x-y plane, with the acceptor layer built on the top surface, Figure S7. The acceptor layer consists of 25 A molecules uniformly distributed with a center to center distance of ~18 Å between the surface-bound phosphonate groups of two adjacent A molecules. The

sensitizer layer consists of 6 P1 molecules, each of which shares the coordination to the respective $\mathrm{Zn^{II}}$ ion with a randomly assigned A molecule. The concentration of acceptors and sensitizers (3:1) correspond to the maximum loading ratio achieved for the photovoltaic measurements. A model with the separation distance of ~9 Å and the same A:Zn-P1 ratio was used for comparison. The entire multilayer construct was embedded in a rectangle solvent box with the same dimension along x and y and a longer length along the surface normal, z, to adequately solvate the construct. Overall, there are 8577 MeCN solvent molecules in the model.

Potential Energy Function Treatment. Classical molecular mechanics energy function form was employed to treat interatomic interactions. Specifically, the CHARMM force field scheme was used. 51 For the TiO₂ assembly, the force field model optimized by Brandt and Lyubartsev was adopted.⁵² In this model, besides standard nonbonded terms among atoms, a corresponding harmonic energy term, the parameters of which were fitted based on the corresponding bonding property, is added to each Ti-O bond. For solvent MeCN molecules and Zn^{II}, the existing CHARMM parameters were used. On the TiO₂ assembly surface, two forms of A molecules were modeled: with and without coordination to Zn-P1. The protonation state of the metal ion coordinated phosphonate and carboxylate groups is still a highly debated topic. 53,34 Here, A molecules with no coordination to Zn-P1 were treated as neutral molecules with both the phosphonate groups doubly protonated. For A molecules coordinated to Zn-P1, the coordinating phosphonate groups were set as being singly protonated, while the surface-anchoring phosphonate groups were still maintained to be doubly protonated (i.e., PO₃H₂). The parameters for A molecules, in which only the ZnII coordinated phosphonate group is deprotonated, were generated through the CGENFF server and the atomic charges were electrostatically fitted based on the standard RESP procedure.⁵⁵ The parameters for sensitizer molecules were customized based on Heme-related and biphenyl-containing molecules in the existing CHARMM parameter set and the atomic charges were electrostatically fitted based on the standard RESP procedure. The particle mesh Ewald (PME) method was used to treat long-range electrostatic interactions. So In real space energy and force calculations, short-range van der Waals and electrostatic interactions were switched off at 12 Å.

MD Simulation Setup. MD simulations were first performed under the *NVT* ensemble for the purpose of initial equilibration. Then the production run was performed under the *NPT* ensemble. The temperature was set as 300 K and the pressure was set as 1 atm; the Nóse–Hoover thermostat⁵⁷ was utilized to maintain the constant temperature and the Langevin piston algorithm⁵⁸ was employed to maintain the constant pressure. The SHAKE algorithm was used to constrain all the bonds that involve hydrogen atoms.⁵⁹ The MD simulation was performed in the CHARMM program with the time step set as 1 fs.⁶⁰

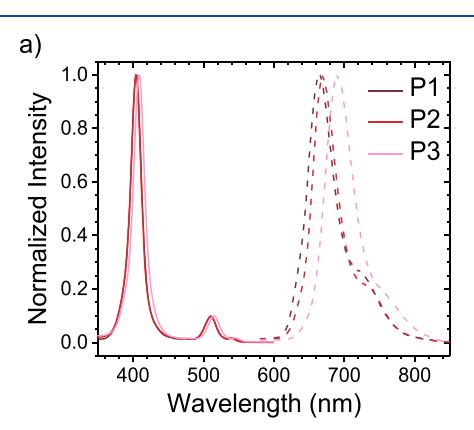
Simulation Data Analysis. Samples collected from MD simulations were used to calculate the distributions and the averages of several important geometric parameters to characterize the A-Zn-P1 bilayer structures. These geometric parameters include directly measurable structural information as depicted in Figure S8. These include: the A tilt angle ($\theta_{tilt,A}$) between the TiO₂ assembly surface normal vector (r_z) and the transition dipole vector r_D as defined across the 9,10 carbons of

anthracene and the Pn tilt angle $(\theta_{tilt,P})$ between the TiO₂ assembly surface normal vector (r_z) and the plane defined by four nitrogen atoms of Pn, and other structural information that may be crucial to determine energy transfer rate. In total, \sim 9.4 ns length of the trajectory was collected for analysis. The first 2.0 ns of the trajectory was considered as the equilibration stage and was discarded from the final analysis.

3. RESULTS AND DISCUSSION

3.1. Sensitizer Synthesis and Photophysics. The platinum(II) meso-tetra(4-carboxyphenyl)porphine (P1) is commercially available but the 3-carboxy (P2) and 2-carboxy (P3) equivalent compounds were synthesized and are reported here for the first time. The unmetalated versions of P2 and P3 were prepared following previously published procedures with minor modifications using Lewis acid-catalyzed condensation between pyrrole and 3-carbomethoxybenzaldehyde⁴² and 2carbomethoxybenzaldehyde, 43 respectively (see Supporting Information for details). Metalation with PtCl₂ in refluxing benzonitrile 44,45 was followed by deesterification with KOH to yield the desired products P2 and P3. It is worth noting that due to the sterically inhibited rotation of the 2-carboxyphenyl groups and in line with previous reports, a statistically driven, mixture of atropisomers for P3 was obtained (i.e., $\alpha,\alpha,\alpha,\alpha$; $\alpha,\alpha,\beta,\beta;$ $\alpha,\alpha,\alpha,\beta;$ and $\alpha,\beta,\alpha,\beta$ in a 1:2:4:1 ratio where α and β are the COOH group above and below the plane, respectively).⁴³ The mixture of atropisomers was used for later experiments without further purification.

The photophysical properties of P1-P3 were measured in N₂-deaerated DMSO, and the results are shown in Figure 2a and summarized in Table 1.



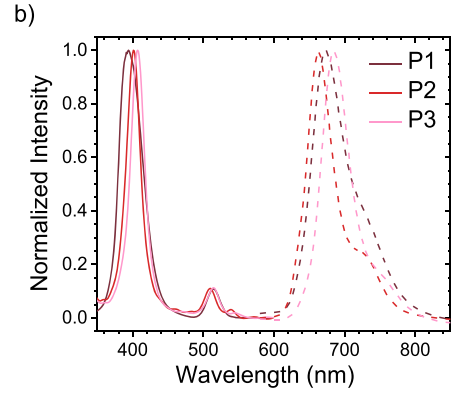


Figure 2. Absorption (solid) and emission (dashed) spectra for P1-**P3** in (a) DMSO and (b) on ZrO_2 in MeCN (λ_{ex} = 410 nm).

All three compounds exhibited photophysical properties typical for platinum(II) porphyrins. 611 That is, strong Soret and Q-band absorption features, deep red emission with tens of microseconds lifetimes and phosphorescent quantum yields of ~1% in DMSO.⁶² The lifetimes and quantum yields for P1-P3 are similar, but there was a subtle bathochromic shift (<50 meV) in the absorption and emission energy of P3 relative to those of P1 and P2.

To study the influence of surface binding, P1-P3 were loaded onto ZrO_2 (~1.2 μ m) by soaking the mesoporous films in a 200 μ M solution of P1-P3 in DMSO for 2 h. Mesoporous ZrO2, as opposed to TiO2, was selected as the substrate because its relatively high conduction band potential inhibits excited state electron transfer from the dyes to the metal oxide surface. 63,64 Thus, emission from P1-P3 can be observed without concerns of quenching by the substrate and the results are shown in Figure 2b and summarized in Table 2.

Table 2. Photophysical Properties of ZrO₂-P1-P3 in N₂-Deaerated MeCN

	λ_{abs} (nm)	$\lambda_{\rm em} (nm)^a$	$\tau (\mu s)^{a,b}$	Φ_{em}	$k_{\rm r} ({\rm s}^{-1})^{c}$	$k_{\rm nr} (s^{-1})^d$
P1	400, 512	670	51	0.016	310	19300
P2	401, 510	665	67	0.038	570	14400
P3	407, 515	686	55	0.016	290	17900

 $^{a}\lambda_{ex}$ = 410 nm. ^bFrom a biexponential fit to the excited state decay at emission peak value with the intensity weighted average reported here. ${}^{c}k_{\rm r} = \Phi/\tau$. ${}^{d}k_{\rm nr} = (1 - \Phi_{\rm FL})/\tau$.

The absorption and emission energies on ZrO₂ were similar to the molecules in DMSO solution (i.e., P3 was hypsochomically shifted relative to P1 and P2) but there was peak broadening and multiexponential kinetics that are typically attributed to the inhomogeneous distribution of surface binding sites. 65 There was also a dramatic increase in weighted average excited state lifetime and emission quantum yield for the surface bound molecules. Given that there is no shift in energetics, we are inclined to attribute the difference in τ and $\Phi_{\rm em}$ for Pn in solution and on ZrO_2 to the change in solvent from DMSO to MeCN, respectively. For example, DMSO coordination to the axial positions of platinum in Pn could be responsible for the order of magnitude increase in the nonradiative decay rate constant. Unfortunately, due to solubility and surface desorption issues, we were unable to find a solvent to make the direct comparison between in solution and on the surface. Herein measurements involving mesoporous metal oxides are performed in MeCN which is the solvent for the TTA-UC solar cells.

It has previously been demonstrated that the porphyrin to TiO₂ photoinduced electron transfer rate is strongly influenced by the porphyrin orientation.⁶⁶ In contrast, the relatively similar trends in photophysical properties of P1-P3 on ZrO₂ and in solution suggests that their intrinsic properties (i.e., absorption and emission) are primarily dictated by the electronics of the porphyrin core. That is, on ZrO2 the molecular orientations are the same, or much more likely, in the absence of electron transfer the photophysical properties are largely independent of the molecular orientation.

3.2. ZrO₂-A-Zn-P*n* **Bilayers.** The bilayer film (ZrO₂-A-Zn-Pn) was prepared by first soaking ZrO_2 in a 200 μM A in DMSO for 48 h. This loading condition ensured a maximum, monolayer surface coverage of 1.0×10^{-7} mol·cm⁻², which equates to an estimated center-to-center inter-A distance of ~9 $\rm \mathring{A}.^{32}~Zn^{II}$ coordination to the nonsurface bound phosphonate groups of A was achieved by soaking the ZrO2-A films in a solution of 400 µM Zn(CH₃COO)₂ in methanol for 30 min. 21,22 ZnII was selected as the metal linking ion because it is photophysically and electrochemically inert under the measurement conditions used here. The ZrO₂-A-Zn-Pn bilayer was then formed by soaking ZrO₂-A-Zn in a 100 μM solution of Pn in DMSO. For comparative purposes, the soaking was continued until a 10:1 ratio of A:Pn was achieved. The fixed ratio enables comparisons between the sensitizer molecules without concerns for variations in porphyrin loading due to differences in binding affinities. The relatively low sensitizer loading also allows us to monitor emission from the annihilator via direct or sensitized excitation with minimized losses due to A to Pn "inner filtering". As an aside, it is worth noting that, in the absence of zinc treatment, minimal porphyrin loading is observed indicating that a bilayer of A-Zn-**P**n is formed rather than codeposition of molecules. ²²

3.2.1. **Pn** to **A** Triplet Energy Transfer. With the bilayer in hand, we then sought to quantify the **Pn** to **A**, interlayer triplet energy transfer rate (TET). TET was monitored using time-resolved emission measurements following our previously published procedures. Briefly, phosphorescence emission decay from the **Pn** ($\lambda_{\rm em}=670~{\rm nm}$) was monitored following 532 nm excitation of two different samples, ZrO₂-**A**-Zn-**Pn** and ZrO₂-**B**-Zn-**Pn**. **B**, terphenyl-4,4"-diylbisphosphonic acid, was introduced as a photo- and electrochemically inert structural analogue of **A** that retains the bilayer structure but does not undergo TET. Rhus, the primary difference between the excited state lifetimes of ZrO₂-**A**-Zn-**Pn** ($\tau_{\rm P(bl)}$) and ZrO₂-**B**-Zn-**Pn** ($\tau_{\rm P}$) is competitive TET emission quenching in the former. The triplet energy transfer rate ($k_{\rm TET}$) and yield ($\Phi_{\rm TET}$) can then be calculated using eqs 1 and 2.

$$k_{TET} = \frac{1}{\tau_{P(bl)}} - \frac{1}{\tau_{P}} \tag{1}$$

$$\Phi_{TET} = 1 - \frac{\tau_{P(bl)}}{\tau_P} \tag{2}$$

As can be seen in Table 3, the TET rate and efficiency are all relatively similar but do decrease in the order P3 > P1 > P2.

Table 3. Rate and Quantum Yields for Interlayer Energy Transfer in ZrO_2 -A-Zn-Pn

	$k_{\text{TET}} (s^{-1})^a$	$\Phi_{\mathrm{TET}}^{}b}$	$k_{\rm ET}~(\rm s^{-1})^c$	$\Phi_{\mathrm{ET}}{}^d$	$J (cm^3 M^{-1})^e$	
P1	6.4×10^{3}	0.25	0.8×10^{7}	0.05	7.2×10^{-11}	
P2	5.6×10^{3}	0.24	1.3×10^{7}	0.09	4.6×10^{-11}	
Р3	7.1×10^{3}	0.31	0.2×10^7	0.02	4.9×10^{-11}	
$\label{eq:kteta} \begin{array}{l} {}^ak_{\mathrm{TET}} = 1/\tau_{\mathrm{P(bl)}} - 1/\tau_{\mathrm{P}}. \ ^b\Phi_{\mathrm{TET}} = 1 - \tau_{\mathrm{P(bl)}}/\tau_{\mathrm{P}}. \ ^ck_{\mathrm{ET}} = 1/\tau_{\mathrm{A(bl)}} - 1/\tau_{\mathrm{A}}, \\ {}^d\Phi_{\mathrm{ET}} = 1 - \tau_{\mathrm{A(bl)}}/\tau_{\mathrm{A}}. \ ^eJ = \int_0^\infty F_{\mathrm{A}}(\lambda)\varepsilon_{\mathrm{S}}(\lambda)\lambda^4 \ \mathrm{d}\lambda/\int_0^\infty F_{\mathrm{A}}(\lambda) \ \mathrm{d}\lambda, \end{array}$						

According to Dexter theory, the rate and efficiency of TET are primarily dictated by the thermodynamic driving-force for electron exchange and the distance and electronic coupling between the donor (P) and acceptor (A) molecules. Given the similar excited state energies of P1–P3 ($\lambda_{\rm em}=665-686$ nm), this similarity is not surprising. However, it is intriguing that sensitizer P3, which has the lowest energy excited state ($\lambda_{\rm em}=686$ nm) also exhibited the fastest ($k_{\rm TET}=7.1\times10^3$) and most efficient ($\Phi_{\rm TET}=31\%$) TET. This suggest that P3 adopts an orientation that is more favorable for TET to occur.

3.2.2. A to Pn Energy Transfer. Following direct excitation or TTA-UC, the singlet excited state of A can be quenched by energy transfer (ET) to Pn. Similar to the method described above for TET, ET was quantified by measuring time-resolved emission at 470 nm after direct excitation of A in films with, ZrO_2 -A-Zn-Pn ($\tau_{A(bi)}$) and without, ZrO_2 -A (τ_A) sensitizer. The ET rate (k_{ET}) and efficiency (Φ_{ET}) were calculated using eqs 3 and 4.

$$k_{ET} = \frac{1}{\tau_{A(bl)}} - \frac{1}{\tau_A} \tag{3}$$

$$\Phi_{ET} = 1 - \frac{\tau_{A(bl)}}{\tau_A} \tag{4}$$

In contrast to the similarities in $k_{\rm TET}$, there was a > 6-fold difference between the highest and lowest **A** to **P**n $k_{\rm ET}$ which decreased in the order **P2** ($k_{\rm ET}=1.3\times10^7~{\rm s}^{-1}$) > **P1** (0.8 × $10^7~{\rm s}^{-1}$) > **P3** (0.2 × $10^7~{\rm s}^{-1}$). Assuming that **A** to **P**n energy transfer occurs via a Förster resonance energy transfer mechanism, 72,73 then the rate of ET is dictated by (1) the fluorescence emission quantum yield of **A** ($\Phi_{\rm FL(A)}$), (2) the overlap integrals between normalized **A** emission and **P**n absorption (J), (3) the dipole orientation factor (κ^2), and (4) the distance between **A** and **P**n. Interestingly, despite **P2** and **P3** having similar J values of 4.6 × 10^{-11} cm³ M⁻¹ and 4.9 × 10^{-11} cm³ M⁻¹, respectively, there was a > 6-fold difference in $k_{\rm ET}$. Because the J values are similar and $\Phi_{\rm FL(A)}$ is expected to be the same in all the bilayer films, then the distance between and relative orientation of **A** and **P**n is likely the primary driver in dictating the differences in $k_{\rm ET}$.

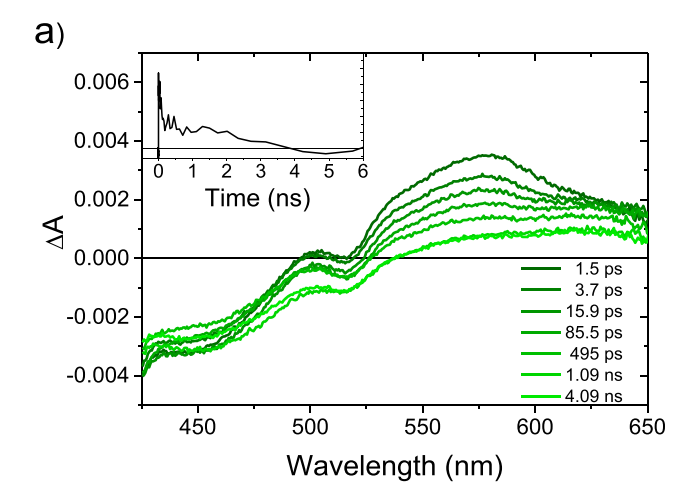
 Φ_{ET} can also be calculated using the steady-state emission intensity from A in ZrO₂-A-Zn-P (I_A(bl)) and ZrO₂-B-Zn-P (I_A) using eq 5.

$$\Phi_{ET} = \frac{I_A - I_{A(bl)}}{I_A} \tag{5}$$

Using this method, $\Phi_{\rm ET}$ decreases in the order P1 (0.50) > P3 (0.49) > P2 (0.37). However, it is important to note that due to the sample angle dependent and highly scattering nature of the films, the consistency and reproducibility of the steady-state emission measurements is much lower ($\pm 10-20\%$) than the time-resolved measurement ($\pm 5\%$). Even accounting for that error, there is a large discrepancy between the $\Phi_{\rm ET}$ measured by time-resolved and steady-state emission. The significantly lower yield calculated by the time-resolved measurement suggests that a large portion of emission quenching is occurring prior to the temporal measurement window (<1 ns) and that $k_{\rm ET}$ may be larger than the values given in Table 3.

To probe the possibility of a subnanosecond **A** to **P***n* energy transfer event, we performed transient absorption spectroscopy on ZrO₂-**A** and ZrO₂-**A**-Zn-**P1** and the results can be seen in Figure 3. For the ZrO₂-**A** sample we see a bleach at <400 nm and a positive ΔA feature from 520 to 700 nm that are consistent with the singlet excited state bleach and absorption of diphenylanthracene. These TA features concomitantly decay with a lifetime of ~2 ns, which is in good agreement with the emission decay kinetics for ZrO₂-**A** ($\tau_{A(em)} = 2.1$ ns). 22

For ZrO_2 -A-Zn-P1 there are similar bleach features, but there is a bathochromic shift in the excited state absorption feature from 560 to 575 nm that occurs in <4 ps (Figure 3b). The lifetime of the lower energy feature is also dramatically



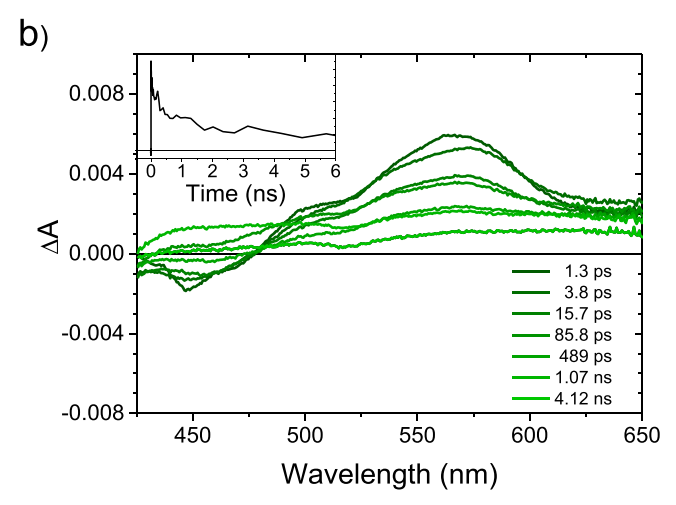


Figure 3. Transient absorption measurements on (a) ZrO_2 -A and (b) ZrO_2 -A-Zn-P ($\lambda_{ex}=360$ nm) in N_2 -deaerated MeCN. Inset: Decay kinetics at 580 nm.

increased with a largely unchanged ΔA through the end of our ~6 ns acquisition window (inset, Figure 3b). On the basis of previously published results, 75 the late time spectra likely have contributions from both 3 Pn (Figure S8) and 3 A* presumably due to the ${}^{1}A^{*}$ to Pn energy transfer, fast intersystem crossing to ${}^{3}\mathbf{P}n^{*}$, and finally ${}^{3}\mathbf{P}n^{*}$ to A TET. Unfortunately, also consistent with previous reports, 75 attempts to deconvolute the species and kinetics with principle component analysis were unsuccessful because of the high spectral overlap of the A and Pn singlet and triplet excited states. Thus, we are unable to assign a rate constant to the quenching of the singlet excited state of A. Nonetheless, the likely presence of ${}^{1}A^{*}$, ${}^{3}Pn^{*}$, and ³A* again indicates that both energy transfer steps in the bilayer are occurring on faster time scales than those listed in Table 3 (i.e., subnanosecond). Ultrafast time-resolved emission measurements will likely be necessary to isolate S₁* emission quenching kinetics and determine the actual A to Pn ET rate constant.

3.3. TTA-UC Solar Cells. Integrated TTA-UC solar cells were fabricated with TiO_2 -A-Zn-Pn as the photoanode, platinum as the counter electrode, and 0.2 M/0.02 M Co^{II} / Co^{III} tris(1,10-phenanthroline) redox mediator in MeCN. The photoanode bilayer films were prepared by using the similar stepwise soaking method, but with TiO_2 as the metal oxide and bubble loading Pn with dry N_2 for 2 h to maximize

the sensitizer absorption resulting in a loading ratio for A:P1, A:P2, and A:P3 of 3:1, 3:1, 6:1, respectively. Current density (J_{sc}) -voltage (V) curves were measured under AM1.5 solar irradiation passed through a 455 nm long-pass filter, to isolate the contribution from TTA-UC, and the results are summarized in Figures S9 and Table S3. Interestingly, although P3 exhibited lower surface loading, the photocurrent contribution from TTA-UC for all three devices was similar $(\sim 10~\mu A~cm^{-2})$. Presumably the $\sim 25\%$ higher $\Phi_{\rm TET}$ and lower $\Phi_{\rm ET}$ (Table 3) for P3 make up for the slightly lower absorbance of the TiO₂-A-Zn-P3 device.

To gain further insights into the photocurrent generation mechanism, J_{sc} was measured with respect to 532 nm excitation intensity (Figure 4) for TiO_2 -A-Zn-Pn devices. All three

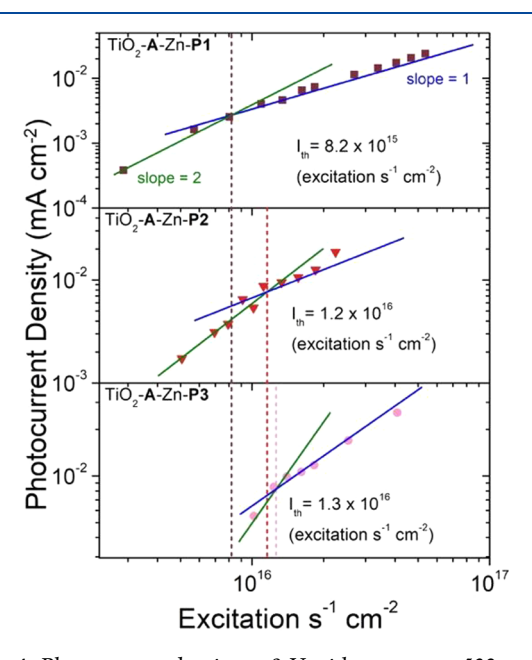


Figure 4. Photocurrent density at 0 V with respect to 532 nm laser intensity for TiO_2 -A-Zn-Pn devices.

devices exhibit quadratic to linear intensity dependence, which is a characteristic feature of TTA-UC. 77,78 The I_{th} values (i.e., the crossover intensity between the quadratic and linear regimes), reported here in excitation events per second (excitation intensity × absorptance), 24 increase in the order of P1 (0.8 × 10 $^{-16}$ ex s $^{-1}$ cm $^{-1}$) < P2 (1.2 × 10 $^{-16}$ ex s $^{-1}$ cm $^{-2}$) \approx P3 (1.3 × 10 $^{-16}$ ex s $^{-1}$ cm $^{-2}$).

The $I_{\rm th}$ value is inversely related to the parameters as described in eq 6:

$$I_{th} = \frac{1}{\Phi_{TET} \times \alpha(E) \times (\tau_{3_A})^2 \times \gamma_{TTA}}$$
(6)

where τ_{3_A} is the triplet excited state lifetime of **A**, Φ_{TET} is the TET efficiency, $\alpha(E)$ is the sensitizer absorption cross-section at 532 nm, and γ_{TTA} is the second-order rate constant for TTA. Using $\tau_A^{3} = 2.02$ ms, and the parameters listed in Table 4, γ_{TTA} was calculated for each device and the results are summarized in Table 4. Remarkably, the γ_{TTA} for all three devices was similar indicating that the adsorption of **P**n has negligible influence on the triplet exciton diffusion or TTA events in the **A** monolayer. The similar γ_{TTA} suggests that in these metal ion linked multilayers, the second layer molecule can be independently tuned to further maximize second layer

Table 4. I_{th} Value, Φ_{TET} , $\alpha(E)$, and the Second-Order Rate Constant for the TTA (γ_{TTA}) for TiO₂-A-Zn-Pn Devices

	$I_{\rm th}~({\rm ex~s^{-1}~cm^{-1}})$	Φ_{TET}	$\alpha(E) (cm^{-1})^a$	$\gamma_{\rm TTA} \left({\rm cm}^3 {\rm s}^{-1}\right)^b$
P1	0.8×10^{-16}	0.25	2976	3.9×10^{-14}
P2	1.2×10^{-16}	0.24	2205	3.7×10^{-14}
P3	1.3×10^{-16}	0.31	1900	3.2×10^{-14}
$a\alpha(E) =$	$= 5700 \times A_{Pn(532 \text{ nr})}$	$_{\rm n}$), $^{b}\gamma_{\rm TTA}$	$= 1/(\Phi_{\rm TET}\alpha(\rm E)\alpha$	$\alpha(\tau_A^{3})^2I_{\rm th}).$

performance and/or interlayer interaction without perturbing the processes in the first layer. This observation may be relevant to metal ion linked water oxidation devices, for example, where cation migration in the first layer is necessary to build up redox equivalents in the second layer catalyst. 40,79,80

3.4. Attenuated Total Reflectance. As described in detail in the Supporting Information, ATR was first used to estimate the surface coverages of A and Pn in the bilayer films and the results are summarized in Table S2. The estimated surface coverage for A on ITO was 2.3×10^{-10} mol/cm². Assuming hexagonal packing and a planar (i.e., atomically flat) ITO surface, this value equates to a center-to-center inter-A distance of ~8.4 Å, which is in good agreement with the ~8.6 Å reported previously for A adsorbed on mesoporous ZrO₂.³² For the adsorption of **P***n* on ITO-**A**-Zn, the surface coverage decreases in the order **P2** $(0.31 \times 10^{-10} \text{ mol/cm}^2) \approx \textbf{P1}$ (0.26 mol/cm^2) $\times 10^{-10} \text{ mol/cm}^2$) > **P3** (0.1 $\times 10^{-10} \text{ mol/cm}^2$). This decrease in loading relative to A likely reflects a combination of reduced number of metal ion binding sites (i.e., TiO₂ vs Zn^{II}), steric restrictions, and the difference in the projected areas of A and Pn. Given the ortho position of the carboxylate, one may expect the projected area being more pronounced for P3, and indeed, we observed the lowest surface coverage for this molecule. For the P1 and P2 bilayers on ITO, the A to Pn loading ratio is \sim 10:1 whereas for P3 it is closer to \sim 20:1. In all cases this more closely resembles the spectroscopic sample loading on ZrO₂ (10:1) than the electrochemical sample loading on TiO₂ (3:1). It is important to acknowledge that, as we will discuss below, this discrepancy in loading ratio could influence the orientation of Pn. We also must note an important disclaimer regarding surface coverage estimates reported here. Based on published AFM images of planar metal oxide-coated glass substrates, the metal oxide surface is not flat.⁸¹ Here, if we assume that the actual surface area is 2-times the nominal surface area, then loading is decreased by half and the A-to-A distance is doubled to ~18 Å. Theoretical calculations below lend further support to the legitimacy of this roughness scalar.

Polarized ATR spectroscopy has also been applied to determine the mean tilt angles of adsorbed molecules on metal oxide surfaces in our previous studies. Because Here, the same methods were used to determine mean tilt angles of the transition dipoles of A ($\theta_{\rm tilt,A}$) and the transition plane of Pn ($\theta_{\rm tilt,P}$) in monolayer and bilayer films on ITO-coated waveguides. The mean tilt angles are listed in Table 5, and schematic depictions of the bilayers are shown in Figure 5.

The mean tilt angle $(\theta_{\rm tilt,A})$ between the transition dipole of A adsorbed to ITO and the surface normal to ITO was $\sim 30^{\circ}$ and had minimal change upon coordination with Zn. This tilt angle, indicative of a predominately out-of-plane orientation in A films, is consistent with studies of phosphonic acid modified molecules adsorbed on ITO and other metal oxide substrates. 48,54

Table 5. Mean tilt angles of A $(\theta_{\rm tilt,A})$ and Pn $(\theta_{\rm tilt,P})$ in monolayer and bilayer films on ITO as determined from ATR.^a

		$\theta_{\text{tilt,A}} \; (\text{deg})$		$\theta_{\text{tilt,P}}$ (deg)
	\mathbf{A}^{b}	A -Zn ^c	A -Zn-Pn ^d	A-Zn-Pn
A-Zn-P1	29 ± 5	30 ± 5	37 ± 7	41 ± 6
A-Zn-P2	29 ± 4	29 ± 5	36 ± 5	64 ± 6
A-Zn-P3	31 ± 5	32 ± 5	34 ± 5	57 ± 6

^aFor **A**, a linear transition dipole aligned along the anthracene short axis (through the 9, 10 carbon atoms) is assumed. ^{84,85} For **Pn**, a circularly polarized dipole in the molecular plane is assumed. ^{86,87} For all cases, n = 3 trials. ^bTilt angle of **A** film before adsorption of Zn and **Pn**. ^cTilt angle of **A** film after adsorption of Zn, before adsorption of **Pn**. ^dTilt angle of **A** film after adsorption of Zn and **Pn**.

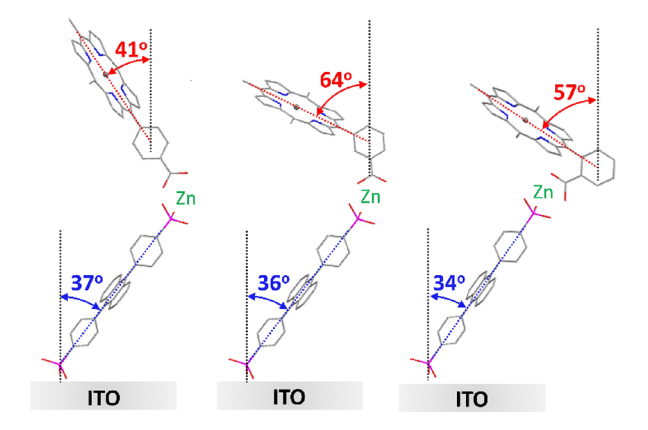


Figure 5. Schematic depictions of the mean orientation of A and Pn in the A-Zn-P1 (left), A-Zn-P2 (middle), and A-Zn-P3 (right) bilayer films on ITO.

To determine the $\theta_{\text{tilt,A}}$ values of **A** in the **A**-Zn-**P***n* bilayers, the spectral contribution of Pn in the 360-450 nm range was subtracted from the A-Zn-Pn spectrum, yielding the spectrum of A-Zn in the bilayer. In all three bilayers, the addition of Pncaused the $\theta_{\text{tilt,A}}$ to increase a few degrees (Table 5). While the magnitude of this change is comparable to the standard deviation of the measurement, the consistency across all samples suggests that this increase in angle is real. It is not unreasonable to suggest that the large size of Pn would force the A molecules into a slightly more in-plane orientation. Regardless, the average orientations of A in the A-Zn-Pn are all ~35°. This observation is consistent with the similar γ_{TTA} across all three TTA-UC solar cells (vida supra) where the cross-surface energy transfer and TTA are dictated by the orientation and intermolecular interaction between molecules in the A monolayer.

The $\theta_{\rm tilt,P}$ between the **P1** molecular plane and surface normal to ITO plane was 41°, while the $\theta_{\rm tilt,P}$ values for **P2** and **P3** films were significantly larger (64° and 57°, respectively). The greater in-plane tilt for **P2** and **P3** is not unexpected given the inherent 60° and 120° change in the angle of the carboxylate binding group in the ortho- and meta-substituted positions relative to the "linear" geometry of the **P1** sensitizer.

Based on the average orientations summarized in Table 5, we have generated a schematic depicting the structure of the molecules in the bilayer, shown in Figure 5. A few important things to note regarding Figure 5. First is that we do not currently have any experimental data to definitively assign a coordination environment around the zinc linking ion. Thus,

the phosphonate—Zn—carboxylate motif depicted in Figure 5 is arbitrary. Second, ATR only provides insights into the orientation of the molecules relative to surface normal and not to each other. Consequently, while all three bilayers in Figure 5 are depicted with the paper/screen being the xz plane that bisects the molecules, the Pn molecule could be rotated around the z-axis, subject to the requirement that its angle relative to the surface normal (e.g., 41° for P1) be maintained.

Nonetheless, these ATR measurements have provided two important milestones for both the bilayer films and the measurement technique. First, the results demonstrate that varying the position of the metal ion binding group can be used to control the average tilt angle of the second layer in metal ion linked multilayers. This result may be instinctively expected, but this is the first experimental data to definitively show that it is true. Being able to control and/or tune the relative angles between molecules in metal ion linked multilayers could have significant implications in controlling energy and electron transfer events for application in solar cells, electrochromics, photocatalysis, molecular p-n junctions, and more. The second key result is that, to our knowledge, this is the first report in which the orientation of two different chromophores in a multilayer thin film have been determined using ATR spectroscopy.

A final important disclaimer regarding these orientation measurements: due to experimental limitations/requirements, the ATR measurements were performed with the bilayer on planar ITO, the spectroscopic measurements on mesoporous $\rm ZrO_2$, and the photocurrent measurements on mesoporous $\rm TiO_2$. It is possible, or even likely, that the different surfaces will impact surface loading and molecular orientations. In fact, preliminary ATR measurements on planar $\rm TiO_2$ suggest that the angle of A decreases to $\sim 20^\circ$ as compare to 30° on ITO. Work is currently underway to systematically investigate the role of the surface composition (e.g., $\rm TiO_2$ vs ITO vs $\rm Al_2O_3$) and roughness (i.e., mesoporous vs planar) on influencing surface loading and the structure of the bilayer.

3.5. Molecular Dynamics Simulation. To supplement results acquired experimentally, we used molecular dynamics simulations to model the TiO₂-A-Zn-P1 bilayer structure to determine the distribution and average angles and distances for the assembly. Briefly, on a TiO₂ crystalline surface, A molecules were uniformly distributed with a center to center distance of ~18 Å. Then P1 was randomly distributed on A-Zn at a A:P1 ratio of 3:1 with MeCN added as the solvent. As expanded upon below, initial models using the experimentally determined ~9 Å spacing of A resulted in an unrealistically high packing density and molecules aligned perpendicular to the substrate suggesting that the 2-fold roughness scalar (*vida supra*) is realistic and necessary surface area correction.

The interatomic interactions were treated with classical molecular mechanics energy function form (details in the Experimental Section) and MD simulations performed at 1 fs time steps for 9.4 ns with the first 2 ns considered as the equilibration stage and discarded from the final analysis. A truncated example of the resulting structure from MD simulations can be seen in Figure 6.

From the results of the simulation, we calculated the distribution and averages for several key parameters relevant to the bilayer structure (Figure S8 and Figure S9) including:

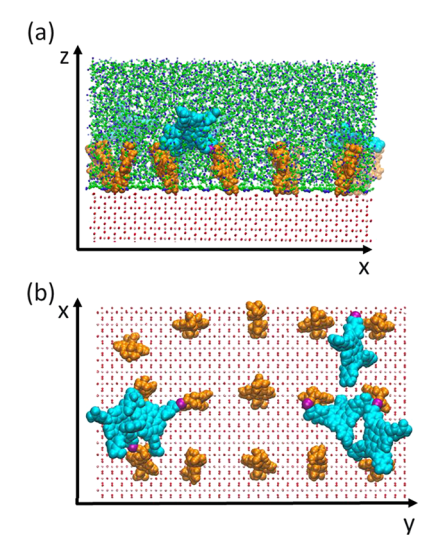


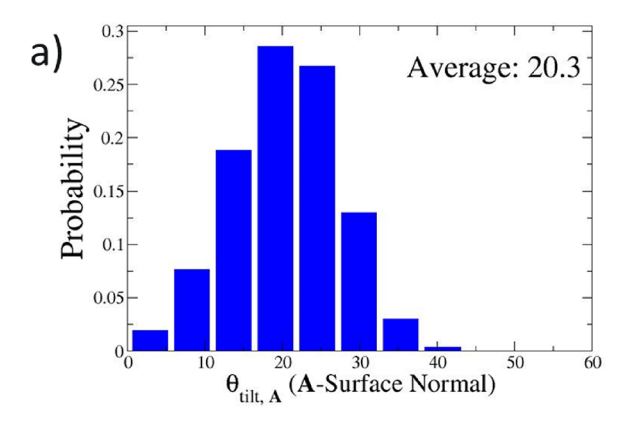
Figure 6. Example results of the MD simulations of TiO_2 -A-Zn-P1 from (a) the front view along the y direction and (b) the top view along the z direction (solvent MeCN molecule are not shown). The TiO_2 assembly and solvent MeCN molecules are represented by the ball and stick model and are colored by atom (C, green; N, blue; O, red; Ti, pink). The A (colored in orange), P (colored in magenta), and Zn^{II} (colored in cyan) moieties are represented by space filling models.

- $\theta_{\text{tilt},A}$: the tilt angle between TiO₂ surface normal vector (r_Z) and the transition dipole of A (r_D) as defined across the 9,10 carbon atoms of anthracene.
- $\theta_{\text{tilt,P}}$: the tilt angle between TiO₂ surface normal vector (r_Z) and the plane of **P1** as defined by the four nitrogen atoms of the porphyrin.
- θ_D : the angle between the transition dipole moment of ET donor **A** (r_D) and r_{DA} .
- θ_A : the angle between the linear transition dipole moment of ET acceptor P1 (r_A) and r_{DA} .
- θ_T : the angle between the r_D and r_A centered on r_{DA} .
- r_{DA} : the center-to-center distance between **A** and **P1**.

The distribution and average values of $\theta_{\rm tilt,A}$, and $\theta_{\rm tilt,P}$ were determined and the results are shown in Figure 7. For $\theta_{\rm tilt,A}$, the mean value calculated from the simulation (20.4°) also suggests that the molecule is tilting relative to the surface normal but the magnitude is lower than that determined by the ATR investigation (37 \pm 7° from Table 5). It is worth noting, however, that the ATR measurements were performed on ITO while the calculations are for TiO2. Remarkably, the calculated 20.4° tilt is in good agreement with our preliminary ATR results suggesting the tilt angle on a TiO2 surface is ~22°, but further work is necessary to confirm there is a metal oxide surface dependence on tilt angle.

The distribution of A tilt angles, which include both lone As and the As in the A-Zn-P1 assembly, is relatively narrow and closely follows a Gaussian distribution (Figure 7a). This is consistent with a general observation from ATR measurements that indicate that the tilt angle for the A layer is insensitive to its coordination environment (i.e., with or without Zn and P1). This also suggests that the angle of A is largely dominated by its interaction with the ${\rm TiO_2}$ surface.

In terms of **P1** tilt angles ($\theta_{\text{tilt,P}}$) the mean value calculated from the simulation, 37.5°, agrees well with the one estimated from the ATR spectroscopy, 41° \pm 6° (Table 5). However, in contrast to **A**, and as can be seen in Figure 7b the distribution



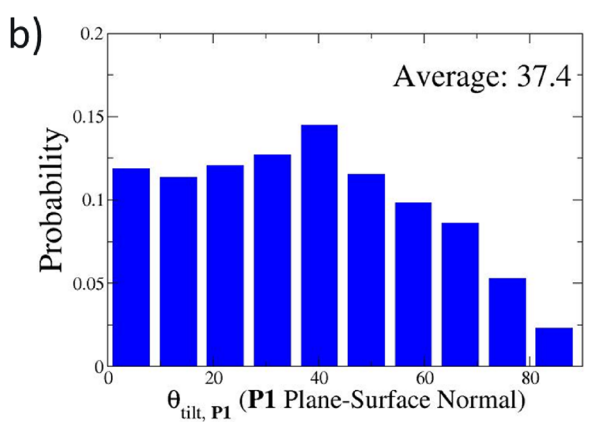


Figure 7. Distribution and average results for (a) $\theta_{\text{tilt,P}}$ for **A**, and (b) $\theta_{\text{tilt,P}}$ for **P1** relative to the TiO₂ surface normal vector r_Z from MD simulations.

is broad with three subensembles, representative of the vertical orientation (centered around 0°), the tilted orientation (centered around 40°), and the near-parallel orientation (centered around 65°). Among these orientation ensembles, the vertical and tilted orientations have comparable populations and the near-parallel orientation has about one-third of the population of the vertical conformation. At a separation of 18 Å, there is considerable flexibility for P1 and a variety of favorable interactions between P1 and surrounding A and P1 layers as well as a random distribution of P1 resulting in adjacent and/or independent P1 molecules; these are the source of the broad orientation distribution for P1. During the simulation, these orientation ensembles also dynamically interconvert between each other. As such, we expect that a change of the separation distance between neighboring A molecules may alter the distribution and mean value of P1 tilt angles. This hypothesis was verified by the comparison simulation with the separation distance decreased to 9 Å. At this distance, A is approximately perpendicular to the TiO₂ surface and the near-parallel orientation ensemble of P1 is not observed. As such, the mean value of P1 tilt angles shifts to 25.5°. The significantly better agreement in average tilt angle for the simulation with an A spacing of 18 Å, as compared to 9 Å, further supports the application of a 2-fold roughness scalar. Additionally, these results indicate that while A remains relatively stagnant, the P1 tilting is a dynamic event with a probability distribution governed by how P1 molecules interact with their neighboring A and P1 molecules. Nonetheless, we can generate a proposed structure of the bilayer based on the

average angles and distances from MD simulations and the results are shown in Figure 8.

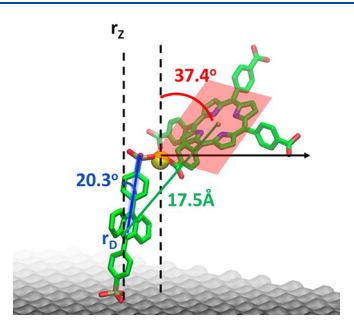


Figure 8. Average structure for the TiO_2 -A-Zn-P1 bilayer from the MD simulations. Features in blue describe the transition dipole vector of the donor molecule (A) as defined across the 9,10 carbons of anthracene and average $\theta_{\rm tilt,A}$ of 20.3° . Red features describe the plane of the acceptor molecule (P1) as defined by the four nitrogen atoms of P1 with the average $\theta_{\rm tilt,P}$ of 37.4°. Last, in green, is the mean center-to-center distance between A and P1, r_{DA} , of 17.5 Å.

With reasonable agreement between MD simulation and ATR measurements, we investigated the geometric parameters that directly determine the rate and efficiency of **A** to **P1** singlet energy transfer which presumably occurs via a FRET mechanism. As previously described, the FRET efficiency is geometrically related to (1) the distance between the centers of **A** (donor) and **P1** (acceptor), r_{DA} , and (2) the angle between the donor (r_D) and acceptor (r_A) transition dipole vectors, θ_T . The porphyrin oscillator can also be described by a circularly polarized dipole or two perpendicular dipoles in the molecular plane but for the sake of simplicity, here θ_T is defined by the angle between vectors r_D and r_A relative to r_{DA} . ^{86–88} A unidirectional vector approximation for the **P1** transition dipole moment may be sufficient here due to linking ion coordination breaking full symmetry and degeneracy of **P1**.

As discussed above, while the distribution of **A** orientations is relatively narrow, there are three orientation subensembles of **P1**. Corresponding to these ensembles, there are three r_{DA} subdistributions centered around 19.0, 16.5, and 14.5 Å (Figure 9a). The donor—acceptor distance strongly correlates with the acceptor **P1** tilt angle, $\theta_{\rm tilt,P}$ that is, larger tilt angles lead to shorter distances. Although large $\theta_{\rm tilt,P}$ values are less populated (Figure 7b), the proportionality of the rate constant for energy transfer $(k_{\rm ET})$ to $1/r_{DA}{}^6$, makes the ET contributions from large tilt angles nontrivial. For instance, the effective r_{DA} distance, defined as $1/\langle 1/r_{DA}{}^6\rangle^{1/6}$, is 15.9 Å; it is lower than the mean r_{DA} distance 17.5 Å, $1/r_{DA}{}^6$ of which only corresponds to about a half of that of the effective r_{DA} distance.

In terms of the relative orientation of **A** and **P1**, θ_T , the distribution is also expectedly broad with the mean value of 108.5° , as shown in Figure 9b. It is notably challenging to deconvolute this broad distribution, particularly how this orientation contributes to $k_{\rm ET}$. As such, we went on to calculate the dipole orientation factor (κ^2) . For $\kappa^2 = (\cos\theta_T - 3\cos\theta_D\cos\theta_A)^2$, θ_D is the angle between vectors r_D and r_{DA} , θ_A is the angle between and vectors r_A and r_{DA} , and θ_T is the angle formed by r_D and r_A when centered on r_{DA} (Figure S9). As shown in Figure 9c, the distribution of κ^2 is also broad. Notably, the distribution favors larger κ^2 values in comparison with that assumed for a free rotating model. The mean κ^2 value is 2.2, or more than 3-fold larger than the value of $^2/_3$ for the

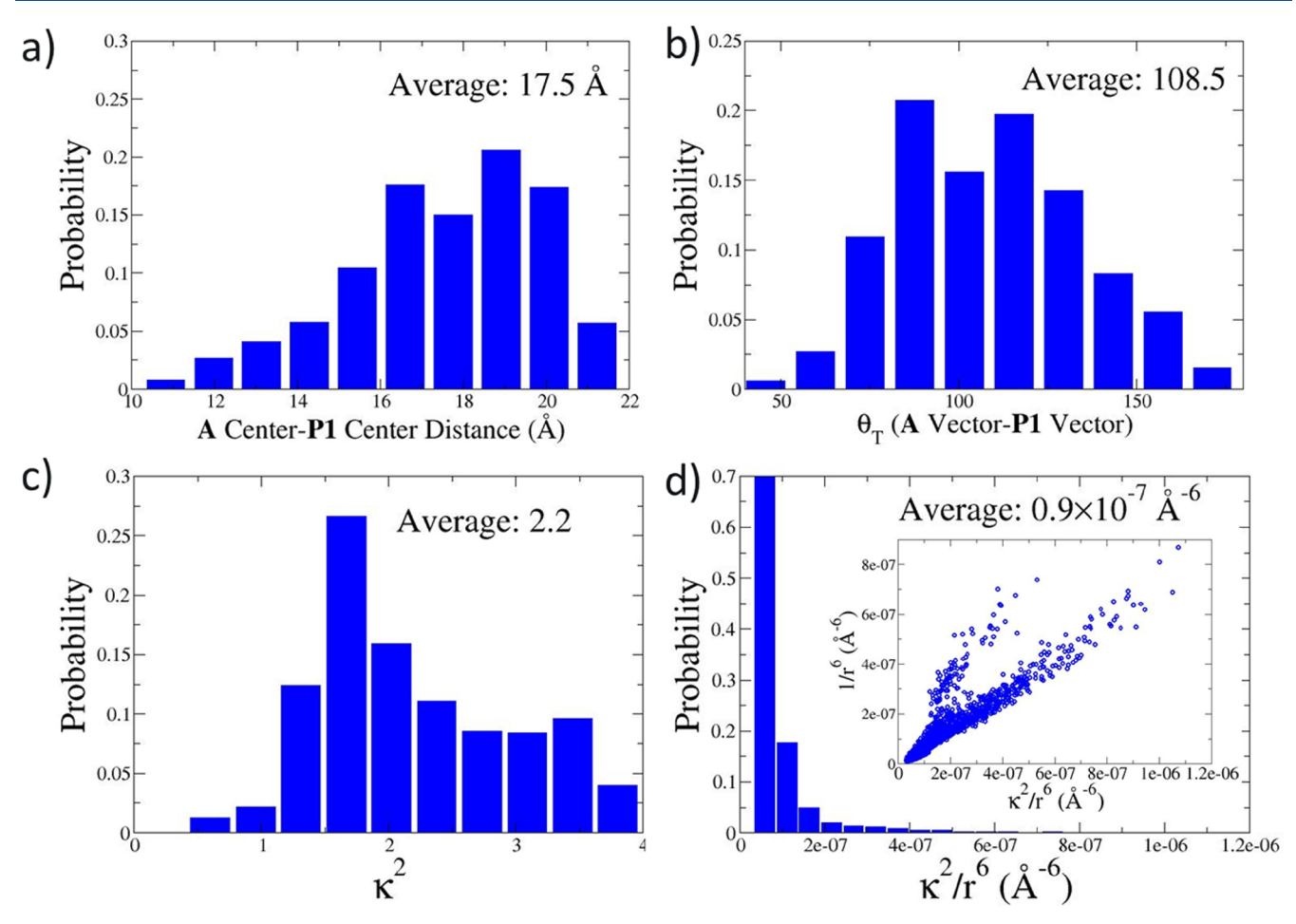


Figure 9. MD simulation results on key geometric parameters responsible for **A** to **P1** ET. (a) Distribution of the distance between the centers of **A** and **P1**, r_{DA} . (b) Distribution of the angle between two transition dipole vectors (θ_T). (c) Distribution of κ^2 . (d) Distribution of κ^2/r_{DA}^6 with noted κ^2 enhancement at short distances (inset).

freely rotating molecules. This further supports that orientation bias imposed by the multilayer structure on metal oxide surfaces can contribute to the enhancement of $k_{\rm ET}$. To better understand the contribution of orientation to energy transfer efficiency, we took advantage of the proportionality $k_{\rm ET} \propto \kappa^2/r_{\rm DA}{}^6$ and calculated the $\kappa^2/r_{\rm DA}{}^6$ distribution and its mean value as shown in Figure 9d. In comparison with $2/3\langle 1/r_{\rm DA}{}^6\rangle$, $\langle \kappa^2/r_{\rm DA}{}^6\rangle$ increases by about 2.2-fold. As demonstrated by the relationship between $1/r_{\rm DA}{}^6$ and $\kappa^2/r_{\rm DA}{}^6$, the shorter $r_{\rm DA}$ is, the larger the orientation enhancement is, reflected in κ^2 (see Figure 9d inset). In summary, both $k_{\rm ET}$ geometry-related determinants are synergistically favored by large P1 tilting, which is driven by the interaction of P1 and the surrounding multilayer structure.

Although in this study we did not carry out MD simulation investigations on P2 and P3, it is reasonable to assume that Pn tilting should also play an essential role in $k_{\rm ET}$. Certainly, due to the different location of the carboxylate group on the mesophenyl rings of P1, P2, and P3, specific interplays between donor—acceptor distance and Pn tilting will be different. Additionally, it is important to note that the above analysis only considers ET between metal ion linked A and P1 molecules. However, at sufficiently high surface packing densities and the appropriate orientation, energy transfer to/from A from/to an adjacent Pn molecule, not coordinated to A, may occur. To more confidently rationalize the difference in energy transfer, we are performing further MD simulation

studies on P2 and P3 and a more thorough analysis of the energy transfer dynamics, which will be reported soon.

4. CONCLUSION

Here we have investigated the influence of the position of the carboxy metal ion binding site (i.e., ortho, meta, para) of Pt(II) tetraphenyl porphyrin (Pn) on energy transfer, photon upconversion, and photocurrent generation in metal ion linked multilayers on metal oxide films. All three porphyrin molecules exhibit similar photophysical properties in solution and on ZrO₂, but when incorporated into a bilayer with a diphosphonic anthracene molecule (A), the films (MO₂-A-Zn-Pn) had notable differences in Pn to/from A energy transfer rates and efficiencies. Given that the energetics of the porphyrins are similar, the differences are attributed to the metal ion binding group influencing the orientation of the Pnrelative to A. Interestingly, from the intensity dependent photocurrent measurement, we find that the second layer Pnmolecule had a minimal influence on γ_{TTA} , indicating that adsorption of Pn does not affect the triplet exciton diffusion or TTA events in the A monolayer.

From polarized attenuated total reflectance measurements of the bilayers on ITO, we found that the orientation of **A** with or without $\mathrm{Zn^{II}}$ is $\sim 30^{\circ}$ relative to the ITO surface normal and only nominally changes to $\sim 35^{\circ}$ upon the coordination of Pn through $\mathrm{Zn^{II}}$. The similar structure of **A** regardless of Pn agrees

well with the similarity of γ_{TTA} which we anticipate being entirely dictated by the coupling between A molecules in the monolayer. In contrast, the average tilt angle of the porphyrin plane varies dramatically from 41° to 64° to 57° for the p-, m-, and o-COOH-substituted porphyrin molecules. The variation in tilt angles for the porphyrin relative to anthracene is likely responsible for the differences in energy transfer rates. It is worth noting that, to our knowledge, this is the first report in which the orientations of two different chromophores in a multilayer thin film have been determined using ATR spectroscopy. This deconvolution procedure could be applied to find the orientation of any two spectroscopically resolvable chromophores on the surface.

To gain further insights into the structure of the bilayer we turned to molecular dynamics (MD) simulation of the MO₂-A-Zn-P1 bilayer where P1 is the para-carboxylated porphyrin. The reasonably good agreement between the tilt angle determined from ATR spectroscopy and the simulation lends support to the calculated structure. Interestingly, while the tilt angle distribution of A was relatively narrow, P1 was found to occupy three different subensembles with near-vertical, tilted, and near-parallel orientations. These different orientations dramatically affected the center-to-center distance and the relative transition dipole moments which are parameters key in dictating energy transfer rates. From the orientation factor (κ^2) and A to P1 distances, which are proportional to the energy transfer rate constant, we find a large distribution in the probability of the energy transfer event with the smaller distance and parallel orientation favoring energy transfer. The broad distribution of orientations suggests that calculating energy transfer rates from the average structure, for example, will not accurately represent the system. Instead, even a small subset of the population with highly favorable energy transfer rates can be the primary driver dictating the energy transfer yield. Additionally, the more than 3-fold higher average κ^2 (2.2) relative to randomly oriented molecules (2/3) indicates that the bilayer film is an effective motif to force favorable orientations for singlet energy transfer. While this type of back energy transfer is productive for photon upconversion, for example, one can envision further optimizing the structure and orientations such that one can maximize or minimize energy transfer as desired. Work to perform more rigorous analyses of energy transfer rates for bilayers containing P1-P3 as well as efforts to understand the influence of the metal oxide on these structures are currently underway.

ASSOCIATED CONTENT

Supporting Information

The Supporting Information is available free of charge at https://pubs.acs.org/doi/10.1021/acs.jpcc.0c08715.

Synthetic procedures for P2 and P3, additional instrumental and experimental details, ATR spectra and isotherms, geometric definitions for ATR and MD simulations, and device performance metrics (PDF)

AUTHOR INFORMATION

Corresponding Authors

Kenneth Hanson — Department of Chemistry & Biochemistry, Florida State University, Tallahassee, Florida 32306, United States; orcid.org/0000-0001-7219-7808; Email: hanson@chem.fsu.edu

- S. Scott Saavedra Department of Chemistry and Biochemistry, University of Arizona, Tucson, Arizona 85721, United States; orcid.org/0000-0002-9946-2664; Email: saavedra@arizona.edu
- Wei Yang Department of Chemistry & Biochemistry and Institute of Molecular Biophysics, Florida State University, Tallahassee, Florida 32306, United States; Email: yyang2@fsu.edu

Authors

- Ashley Arcidiacono Department of Chemistry & Biochemistry, Florida State University, Tallahassee, Florida 32306, United States
- Yan Zhou Department of Chemistry & Biochemistry, Florida State University, Tallahassee, Florida 32306, United States
- **Wendi Zhang** Department of Chemistry and Biochemistry, University of Arizona, Tucson, Arizona 85721, United States
- Jeffrey O. Ellison Department of Chemistry & Biochemistry, Florida State University, Tallahassee, Florida 32306, United States
- Suliman Ayad Department of Chemistry & Biochemistry, Florida State University, Tallahassee, Florida 32306, United States
- Erica S. Knorr Department of Chemistry & Biochemistry, Florida State University, Tallahassee, Florida 32306, United States
- Autumn N. Peters Department of Chemistry & Biochemistry, Florida State University, Tallahassee, Florida 32306, United States
- Lianqing Zheng Institute of Molecular Biophysics, Florida State University, Tallahassee, Florida 32306, United States

Complete contact information is available at: https://pubs.acs.org/10.1021/acs.jpcc.0c08715

Author Contributions

¹A.A. and Y.Z. contributed equally to the work.

Notes

The authors declare no competing financial interest.

ACKNOWLEDGMENTS

Photon upconversion measurements were supported by the National Science Foundation under Grant No. DMR-1752782. Structural characterization of the bilayer was supported by the Army Research Office under Grant No. W911NF-19-1-0357. All ATR data was collected in the W.M. Keck Center for Nano-Scale Imaging in the Department of Chemistry and Biochemistry at the University of Arizona. This instrument was supported as part of the Center for Interface Science: Solar-Electric Materials (CIS:SEM), an Energy Frontier Research Center funded by the U.S. Department of Energy, Office of Science, Office of Basic Energy Sciences under Award No. DE-SC0001084. A.N.P. was supported by the NSF-REU program under Grant No. CHE-1659661. Transient absorption measurements were performed on a spectrometer supported by the National Science Foundation under Grant No. CHE-1919633. MD simulation efforts were supported by the National Institute of Health under Grant R01GM111886.

REFERENCES

(1) Zhou, J.; Liu, Q.; Feng, W.; Sun, Y.; Li, F. Upconversion Luminescent Materials: Advances and Applications. *Chem. Rev.* **2015**, 115, 395–465.

- (2) Kim, H.-i.; Weon, S.; Kang, H.; Hagstrom, A. L.; Kwon, O. S.; Lee, Y.-S.; Choi, W.; Kim, J.-H. Plasmon-Enhanced Sub-Bandgap Photocatalysis via Triplet-Triplet Annihilation Upconversion for Volatile Organic Compound Degradation. Environ. Sci. Technol. 2016, 50, 11184-11192.
- (3) Zhang, P.; Steelant, W.; Kumar, M.; Scholfield, M. Versatile Photosensitizers for Photodynamic Therapy at Infrared Excitation. J. Am. Chem. Soc. 2007, 129, 4526-4527.
- (4) Cheng, Y. Y.; Fuckel, B.; MacQueen, R. W.; Khoury, T.; Clady, R. G. C. R.; Schulze, T. F.; Ekins-Daukes, N. J.; Crossley, M. J.; Stannowski, B.; Lips, K.; et al. Improving the Light-harvesting of Amorphous Silicon Solar Cells with Photochemical Upconversion. Energy Environ. Sci. 2012, 5, 6953-6959.
- (5) Nattestad, A.; Cheng, Y. Y.; MacQueen, R. W.; Schulze, T. F.; Thompson, F. W.; Mozer, A. J.; Fückel, B.; Khoury, T.; Crossley, M. J.; Lips, K.; et al. Dye-Sensitized Solar Cell with Integrated Triplet-Triplet Annihilation Upconversion System. J. Phys. Chem. Lett. 2013, 4, 2073-2078.
- (6) Singh-Rachford, T. N.; Castellano, F. N. Photon Upconversion Based on Sensitized Triplet-triplet Annihilation. Coord. Chem. Rev. 2010, 254, 2560-2573.
- (7) Simon, Y. C.; Weder, C. Low-power Photon Upconversion through Triplet-triplet Annihilation in Polymers. J. Mater. Chem. **2012**, 22, 20817-20830.
- (8) Schulze, T. F.; Schmidt, T. W. Photochemical Upconversion: Present Status and Prospects for its Application to Solar Energy Conversion. Energy Environ. Sci. 2015, 8, 103-125.
- (9) Yanai, N.; Kimizuka, N. Recent Emergence of Photon Upconversion based on Triplet Energy Migration in Molecular Assemblies. Chem. Commun. 2016, 52, 5354-5370.
- (10) Gray, V.; Moth-Poulsen, K.; Albinsson, B.; Abrahamsson, M. Towards Efficient Solid-state Triplet-triplet Annihilation based Photon Upconversion: Supramolecular, Macromolecular and Selfassembled Systems. Coord. Chem. Rev. 2018, 362, 54-71.
- (11) Kimizuka, N.; Yanai, N.; Morikawa, M.-a. Photon Upconversion and Molecular Solar Energy Storage by Maximizing the Potential of Molecular Self-Assembly. Langmuir 2016, 32, 12304-12322.
- (12) Ogawa, T.; Yanai, N.; Monguzzi, A.; Kimizuka, N. Highly Efficient Photon Upconversion in Self-Assembled Light-Harvesting Molecular Systems. Sci. Rep. 2015, 5, 10882.
- (13) Gray, V.; Börjesson, K.; Dzebo, D.; Abrahamsson, M.; Albinsson, B.; Moth-Poulsen, K. Porphyrin-Anthracene Complexes: Potential in Triplet-Triplet Annihilation Upconversion. J. Phys. Chem. C 2016, 120, 19018-19026.
- (14) Gray, V.; Kucukoz, B.; Edhborg, F.; Abrahamsson, M.; Moth-Poulsen, K.; Albinsson, B. Singlet and Triplet Energy Transfer Dynamics in Self-assembled Axial Porphyrin-anthracene Complexes: towards Supra-molecular Structures for Photon Upconversion. Phys. Chem. Chem. Phys. 2018, 20, 7549-7558.
- (15) Fan, C.; Wu, W.; Chruma, J. J.; Zhao, J.; Yang, C. Enhanced Triplet-Triplet Energy Transfer and Upconversion Fluorescence through Host-Guest Complexation. J. Am. Chem. Soc. 2016, 138, 15405-15412.
- (16) Ishiba, K.; Morikawa, M.-a.; Chikara, C.; Yamada, T.; Iwase, K.; Kawakita, M.; Kimizuka, N. Photoliquefiable Ionic Crystals: A Phase Crossover Approach for Photon Energy Storage Materials with Functional Multiplicity. Angew. Chem., Int. Ed. 2015, 54, 1532-1536.
- (17) Ahmad, S.; Liu, J.; Gong, C.; Zhao, J.; Sun, L. Photon Up-Conversion via Epitaxial Surface-Supported Metal-Organic Framework Thin Films with Enhanced Photocurrent. ACS Appl. Energy Mater. 2018, 1, 249-253.
- (18) Park, J.; Xu, M.; Li, F.; Zhou, H.-C. 3D Long-Range Triplet Migration in a Water-Stable Metal-Organic Framework for Upconversion-Based Ultralow-Power in Vivo Imaging. J. Am. Chem. Soc. 2018, 140, 5493-5499.
- (19) Hanson, K.; Torelli, D. A.; Vannucci, A. K.; Brennaman, M. K.; Luo, H.; Alibabaei, L.; Song, W.; Ashford, D. L.; Norris, M. R.; Glasson, C. R. K.; et al. Self-Assembled Bilayer Films of Ruthenium-(II)/Polypyridyl Complexes through Layer-by-Layer Deposition on

- Nanostructured Metal Oxides. Angew. Chem., Int. Ed. 2012, 51, 12782-12785.
- (20) Robb, A. J.; Knorr, E. S.; Watson, N.; Hanson, K. Metal Ion Linked Multilayers on Mesoporous Substrates: Energy/electron Transfer, Photon upconversion, and more. J. Photochem. Photobiol., A 2020, 390, 112291.
- (21) Hill, S. P.; Dilbeck, T.; Baduell, E.; Hanson, K. Integrated Photon Upconversion Solar Cell via Molecular Self-Assembled Bilayers. ACS Energy Lett. 2016, 1, 3-8.
- (22) Hill, S. P.; Banerjee, T.; Dilbeck, T.; Hanson, K. Photon Upconversion and Photocurrent Generation via Self-Assembly at Organic-Inorganic Interfaces. J. Phys. Chem. Lett. 2015, 6, 4510-
- (23) Dilbeck, T.; Hanson, K. Molecular Photon Upconversion Solar Cells Using Multilayer Assemblies: Progress and Prospects. J. Phys. Chem. Lett. 2018, 9, 5810-5821.
- (24) Zhou, Y.; Castellano, F. N.; Schmidt, T. W.; Hanson, K. On the Quantum Yield of Photon Upconversion via Triplet-Triplet Annihilation. ACS Energy Lett. 2020, 5, 2322-2326.
- (25) Beery, D.; Wheeler, J. P.; Arcidiacono, A.; Hanson, K. CdSe Quantum Dot Sensitized Molecular Photon Upconversion Solar Cells. ACS Appl. Energy Mater. 2020, 3, 29-37.
- (26) Baluschev, S.; Yakutkin, V.; Miteva, T.; Wegner, G.; Roberts, T.; Nelles, G.; Yasuda, A.; Chernov, S.; Aleshchenkov, S.; Cheprakov, A. A General Approach for Non-coherently Excited Annihilation Upconversion: Transforming the Solar-spectrum. New J. Phys. 2008, 10, 013007.
- (27) Tayebjee, M. J. Y.; McCamey, D. R.; Schmidt, T. W. Beyond Shockley-Queisser: Molecular Approaches to High-Efficiency Photovoltaics. J. Phys. Chem. Lett. 2015, 6, 2367-2378.
- (28) Trupke, T.; Green, M. A.; Würfel, P. Improving Solar Cell Efficiencies by Down-Conversion of High-Energy Photons. J. Appl. Phys. 2002, 92, 1668-1674.
- (29) Zhou, Y.; Ruchlin, C.; Robb, A. J.; Hanson, K. Singlet Sensitization-Enhanced Upconversion Solar Cells via Self-Assembled Trilayers. ACS Energy Lett. 2019, 4, 1458-1463.
- (30) Frazer, L.; Gallaher, J. K.; Schmidt, T. W. Optimizing the Efficiency of Solar Photon Upconversion. ACS Energy Lett. 2017, 2, 1346-1354.
- (31) Zhou, Y.; Hill, S. P.; Hanson, K. Influence of Meta- and Paraphosphonated Diphenylanthracene on Photon Upconversion in Selfassembled Bilayers. J. Photonics Energy 2018, 8, 1-11.
- (32) Zhou, Y.; Ayad, S.; Ruchlin, C.; Posey, V.; Hill, S. P.; Wu, Q.; Hanson, K. Examining the Role of Acceptor Molecule Structure in Self-assembled Bilayers: Surface loading, Stability, Energy Transfer, and Upconverted Emission. Phys. Chem. Chem. Phys. 2018, 20, 20513-20524.
- (33) Zhao, J.; Ji, S.; Guo, H. Triplet-triplet Annihilation based Upconversion: From Triplet Sensitizers and Triplet Acceptors to Upconversion Quantum Yields. RSC Adv. 2011, 1, 937-950.
- (34) Yanai, N.; Kimizuka, N. New Triplet Sensitization Routes for Photon Upconversion: Thermally Activated Delayed Fluorescence Molecules, Inorganic Nanocrystals, and Singlet-to-Triplet Absorption. Acc. Chem. Res. 2017, 50, 2487-2495.
- (35) Moor, K.; Kim, J.-H.; Snow, S.; Kim, J.-H. [C70] Fullerenesensitized Triplet-triplet Annihilation Upconversion. Chem. Commun. 2013, 49, 10829-10831.
- (36) Pedrini, J.; Monguzzi, A.; Meinardi, F. Cascade Sensitization of Triplet-triplet Annihilation based Photon Upconversion at Sub-solar Irradiance. Phys. Chem. Chem. Phys. 2018, 20, 9745-9750.
- (37) Dilbeck, T.; Hill, S. P.; Hanson, K. Harnessing Molecular Photon Upconversion at Sub-solar Irradiance using Dual Sensitized Self-assembled Trilayers. J. Mater. Chem. A 2017, 5, 11652-11660.
- (38) Wang, J. C.; Murphy, I. A.; Hanson, K. Modulating Electron Transfer Dynamics at Dye-Semiconductor Interfaces via Self-Assembled Bilayers. J. Phys. Chem. C 2015, 119, 3502-3508.
- (39) Heimer, T. A.; D'Arcangelis, S. T.; Farzad, F.; Stipkala, J. M.; Meyer, G. J. An Acetylacetonate-Based Semiconductor-Sensitizer Linkage. Inorg. Chem. 1996, 35, 5319-5324.

- (40) Song, W.; Glasson, C. R. K.; Luo, H.; Hanson, K.; Brennaman, M. K.; Concepcion, J. J.; Meyer, T. J. Photoinduced Stepwise Oxidative Activation of a Chromophore—Catalyst Assembly on TiO2. *J. Phys. Chem. Lett.* **2011**, *2*, 1808–1813.
- (41) Ogunsolu, O. O.; Murphy, I. A.; Wang, J. C.; Das, A.; Hanson, K. Energy and Electron Transfer Cascade in Self-Assembled Bilayer Dye-Sensitized Solar Cells. ACS Appl. Mater. Interfaces 2016, 8, 28633–28640.
- (42) Lipstman, S.; Goldberg, I. Supramolecular Crystal Chemistry with Porphyrin Tinkertoys. Hydrogen-Bonding and Coordination Networks with the "Chair" and "Table" Conformers of Tetra(3-carboxyphenyl)porphyrin. Cryst. Growth Des. 2013, 13, 942–952.
- (43) Leondiadis, L.; Momenteau, M. 5,10,15,20-Tetrakis (.alpha.,.alpha.,.alpha.,.alpha.-o-(N-tert-butyl-carbamoyl)phenyl)porphyrin: Synthesis and Redox Properties of Zinc(II) and Copper(II) Complexes. J. Org. Chem. 1989, 54, 6135–6138.
- (44) Mink, L. M.; Neitzel, M. L.; Bellomy, L. M.; Falvo, R. E.; Boggess, R. K.; Trainum, B. T.; Yeaman, P. Platinum(II) and Platinum(IV) Porphyrin Complexes: Synthesis, Characterization, and Electrochemistry. *Polyhedron* 1997, 16, 2809–2817.
- (45) Drouet, S.; Paul-Roth, C. O.; Fattori, V.; Cocchi, M.; Williams, J. A. G. Platinum and Palladium Complexes of Fluorenyl Porphyrins as Red Phosphors for Light-emitting Devices. *New J. Chem.* **2011**, 35 (2), 438–444.
- (46) Gallagher, L. A.; Serron, S. A.; Wen, X.; Hornstein, B. J.; Dattelbaum, D. M.; Schoonover, J. R.; Meyer, T. J. Photoelectrochemistry on RuII-2,2'-bipyridine-phosphonate-Derivatized TiO₂ with the I₃⁻/I⁻ and Quinone/Hydroquinone Relays. Design of Photoelectrochemical Synthesis Cells. *Inorg. Chem.* **2005**, *44*, 2089–2097
- (47) Araci, Z. O.; Shallcross, C. R.; Armstrong, N. R.; Saavedra, S. S. Potential-Modulated Attenuated Total Reflectance Characterization of Charge Injection Processes in Monolayer-Tethered CdSe Nanocrystals. *J. Phys. Chem. Lett.* **2010**, *1*, 1900–1905.
- (48) Zheng, Y.; Giordano, A. J.; Shallcross, R. C.; Fleming, S. R.; Barlow, S.; Armstrong, N. R.; Marder, S. R.; Saavedra, S. S. Surface Modification of Indium—Tin Oxide with Functionalized Perylene Diimides: Characterization of Orientation, Electron-Transfer Kinetics and Electronic Structure. J. Phys. Chem. C 2016, 120, 20040—20048.
- (49) Mendes, S. B.; Bradshaw, J. T.; Saavedra, S. S. Technique for Determining the Angular Orientation of Molecules Bound to the Surface of an Arbitrary Planar Optical Waveguide. *Appl. Opt.* **2004**, 43, 70–78.
- (50) Bowman, D. N.; Blew, J. H.; Tsuchiya, T.; Jakubikova, E. Elucidating Band-Selective Sensitization in Iron(II) Polypyridine-TiO2 Assemblies. *Inorg. Chem.* **2013**, *52*, 8621–8628.
- (51) MacKerell, A. D.; Bashford, D.; Bellott, M.; Dunbrack, R. L.; Evanseck, J. D.; Field, M. J.; Fischer, S.; Gao, J.; Guo, H.; Ha, S.; et al. All-Atom Empirical Potential for Molecular Modeling and Dynamics Studies of Proteins. *J. Phys. Chem. B* **1998**, *102*, 3586–3616.
- (52) Brandt, E. G.; Lyubartsev, A. P. Systematic Optimization of a Force Field for Classical Simulations of TiO2—Water Interfaces. *J. Phys. Chem. C* **2015**, *119*, 18110—18125.
- (53) Thomas, A. G.; Syres, K. L. Adsorption of Organic Molecules on Rutile TiO₂ and Anatase TiO₂ Single Crystal Surfaces. *Chem. Soc. Rev.* **2012**, *41*, 4207–4217.
- (54) Paniagua, S. A.; Giordano, A. J.; Smith, O. N. L.; Barlow, S.; Li, H.; Armstrong, N. R.; Pemberton, J. E.; Brédas, J.-L.; Ginger, D.; Marder, S. R. Phosphonic Acids for Interfacial Engineering of Transparent Conductive Oxides. *Chem. Rev.* **2016**, *116*, 7117–7158.
- (55) Bayly, C. I.; Cieplak, P.; Cornell, W.; Kollman, P. A. A Wellbehaved Electrostatic Potential based Method using Charge Restraints for Deriving Atomic Charges: the RESP Model. *J. Phys. Chem.* **1993**, 97, 10269–10280.
- (56) Darden, T.; York, D.; Pedersen, L. Particle Mesh Ewald: An N-log(N) Method for Ewald Sums in Large Systems. *J. Chem. Phys.* **1993**, 98, 10089–10092.
- (57) Nosé, S. A Unified Formulation of the Constant Temperature Molecular Dynamics Methods. *J. Chem. Phys.* **1984**, *81*, 511–519.

- (58) Feller, S. E.; Zhang, Y.; Pastor, R. W.; Brooks, B. R. Constant Pressure Molecular Dynamics Simulation: The Langevin Piston Method. *J. Chem. Phys.* **1995**, *103*, 4613–4621.
- (59) Ryckaert, J.-P.; Ciccotti, G.; Berendsen, H. J. C. Numerical Integration of the Cartesian Equations of Motion of a System with Constraints: Molecular Dynamics of n-alkanes. *J. Comput. Phys.* **1977**, 23, 327–341.
- (60) Brooks, B. R.; Brooks, C. L., Iii; Mackerell, A. D., Jr; Nilsson, L.; Petrella, R. J.; Roux, B.; Won, Y.; Archontis, G.; Bartels, C.; Boresch, S.; et al. CHARMM: The Biomolecular Simulation Program. *J. Comput. Chem.* **2009**, *30*, 1545–1614.
- (61) Chen, P.; Finikova, O. S.; Ou, Z.; Vinogradov, S. A.; Kadish, K. M. Electrochemistry of Platinum(II) Porphyrins: Effect of Substituents and π -Extension on Redox Potentials and Site of Electron Transfer. *Inorg. Chem.* **2012**, *51*, 6200–6210.
- (62) Bansal, A. K.; Holzer, W.; Penzkofer, A.; Tsuboi, T. Absorption and Emission Spectroscopic Characterization of Platinum-Octaethyl-Porphyrin (PtOEP). *Chem. Phys.* **2006**, *330*, 118–129.
- (63) Butler, M. A.; Ginley, D. S. Prediction of Flatband Potentials at Semiconductor-Electrolyte Interfaces from Atomic Electronegativities. *J. Electrochem. Soc.* **1978**, *125*, 228–232.
- (64) Tachibana, Y.; Moser, J. E.; Grätzel, M.; Klug, D. R.; Durrant, J. R. Subpicosecond Interfacial Charge Separation in Dye-Sensitized Nanocrystalline Titanium Dioxide Films. *J. Phys. Chem.* **1996**, *100*, 20056–20062.
- (65) Durrant, J. R.; Haque, S. A.; Palomares, E. Towards Optimisation of Electron Transfer Processes in Dye Sensitised Solar Cells. *Coord. Chem. Rev.* **2004**, 248, 1247–1257.
- (66) Hart, A. S.; Kc, C. B.; Gobeze, H. B.; Sequeira, L. R.; D'Souza, F. Porphyrin-Sensitized Solar Cells: Effect of Carboxyl Anchor Group Orientation on the Cell Performance. *ACS Appl. Mater. Interfaces* **2013**, *5*, 5314–5323.
- (67) Wang, J. C.; Ogunsolu, O. O.; Sykora, M.; Hanson, K. Elucidating the Role of the Metal Linking Ion on the Excited State Dynamics of Self-Assembled Bilayers. *J. Phys. Chem. C* **2018**, *122*, 9835–9842.
- (68) Wang, J. C.; Violette, K.; Ogunsolu, O. O.; Cekli, S.; Lambers, E.; Fares, H. M.; Hanson, K. Self-Assembled Bilayers on Nanocrystalline Metal Oxides: Exploring the Non-Innocent Nature of the Linking Ions. *Langmuir* **2017**, 33, 9609–9619.
- (69) Dilbeck, T.; Wang, J. C.; Zhou, Y.; Olsson, A.; Sykora, M.; Hanson, K. Elucidating the Energy and Electron Transfer Dynamics of Photon Upconversion in Self-Assembled Bilayers. *J. Phys. Chem. C* **2017**, *121*, 19690–19698.
- (70) Dexter, D. L. A Theory of Sensitized Luminescence in Solids. *J. Chem. Phys.* **1953**, 21, 836–850.
- (71) Giribabu, L.; Ashok Kumar, A.; Neeraja, V.; Maiya, B. Orientation Dependence of Energy Transfer in an Anthracene–Porphyrin Donor–Acceptor System. *Angew. Chem.* **2001**, *113*, 3733–3736.
- (72) Lakowicz, J. R. Principles of fluorescence spectroscopy; 3rd ed.; Springer: New York, 2006.
- (73) Förster, T. 10th Spiers Memorial Lecture. Transfer Mechanisms of Electronic Excitation. *Discuss. Faraday Soc.* **1959**, 27, 7–17.
- (74) Dilbeck, T.; Wang, J. C.; Zhou, Y.; Olsson, A.; Sykora, M.; Hanson, K. Elucidating the Energy- and Electron-Transfer Dynamics of Photon Upconversion in Self-Assembled Bilayers. *J. Phys. Chem. C* **2017**, *121* (36), 19690–19698.
- (75) Lang, B.; Mosquera-Vázquez, S.; Lovy, D.; Sherin, P.; Markovic, V.; Vauthey, E. Broadband Ultraviolet-visible Transient Absorption Spectroscopy in the Nanosecond to Microsecond Time Domain with Sub-nanosecond Time Resolution. *Rev. Sci. Instrum.* **2013**, *84*, 073107.
- (76) Hill, S. P.; Hanson, K. Harnessing Molecular Photon Upconversion in a Solar Cell at Sub-solar Irradiance: Role of the Redox Mediator. *J. Am. Chem. Soc.* **2017**, *139*, 10988–10991.
- (77) Monguzzi, A.; Mezyk, J.; Scotognella, F.; Tubino, R.; Meinardi, F. Upconversion-Induced Fluorescence in Multicomponent Systems:

- Steady-state Excitation Power Threshold. Phys. Rev. B: Condens. Matter Mater. Phys. 2008, 78, 195112.
- (78) Haefele, A.; Blumhoff, J.; Khnayzer, R. S.; Castellano, F. N. Getting to the (Square) Root of the Problem: How to Make Noncoherent Pumped Upconversion Linear. *J. Phys. Chem. Lett.* **2012**, 3, 299–303.
- (79) Song, W.; Ito, A.; Binstead, R. A.; Hanson, K.; Luo, H.; Brennaman, M. K.; Concepcion, J. J.; Meyer, T. J. Accumulation of Multiple Oxidative Equivalents at a Single Site by Cross-Surface Electron Transfer on TiO₂. *J. Am. Chem. Soc.* **2013**, *135*, 11587–11594.
- (80) Bettis, S. E.; Hanson, K.; Wang, L.; Gish, M. K.; Concepcion, J. J.; Fang, Z.; Meyer, T. J.; Papanikolas, J. M. Photophysical Characterization of a Chromophore/Water Oxidation Catalyst Containing a Layer-by-Layer Assembly on Nanocrystalline TiO₂ Using Ultrafast Spectroscopy. *J. Phys. Chem. A* **2014**, *118*, 10301–10308.
- (81) Ehamparam, R.; Oquendo, L. E.; Liao, M. W.; Brynnel, A. K.; Ou, K.-L.; Armstrong, N. R.; McGrath, D. V.; Saavedra, S. S. Axially Bound Ruthenium Phthalocyanine Monolayers on Indium Tin Oxide: Structure, Energetics, and Charge Transfer Properties. ACS Appl. Mater. Interfaces 2017, 9, 29213–29223.
- (82) Lin, H.-C.; MacDonald, G. A.; Shi, Y.; Polaske, N. W.; McGrath, D. V.; Marder, S. R.; Armstrong, N. R.; Ratcliff, E. L.; Saavedra, S. S. Influence of Molecular Orientation on Charge-Transfer Processes at Phthalocyanine/Metal Oxide Interfaces and Relationship to Organic Photovoltaic Performance. *J. Phys. Chem. C* **2015**, *119*, 10304–10313.
- (83) Lin, H.-C.; Polaske, N. W.; Oquendo, L. E.; Gliboff, M.; Knesting, K. M.; Nordlund, D.; Ginger, D. S.; Ratcliff, E. L.; Beam, B. M.; Armstrong, N. R.; McGrath, D. V.; Saavedra, S. S. Electron-Transfer Processes in Zinc Phthalocyanine—Phosphonic Acid Monolayers on ITO: Characterization of Orientation and Charge-Transfer Kinetics by Waveguide Spectroelectrochemistry. *J. Phys. Chem. Lett.* **2012**, *3*, 1154—1158.
- (84) Inoue, H.; Hoshi, T.; Masamoto, T.; Shiraishi, J.; Tanizaki, Y. Dichroic Spectra of Anthracene, Acridine and Phenazine in Stretched PVA sheets. *Ber. Bunsen Ges. Phys. Chem.* **1971**, 75 (5), 441–446.
- (85) Norden, B.; Lindblom, G.; Jonas, I. Linear Dichroism Spectroscopy as a Tool for Studying Molecular Orientation in Model Membrane Systems. *J. Phys. Chem.* **19**77, *81*, 2086–2093.
- (86) Gouterman, M. Spectra of porphyrins. J. Mol. Spectrosc. 1961, 6, 138–163.
- (87) Shelnutt, J. A.; Ortiz, V. Substituent Effects on the Electronic Structure of Metalloporphyrins: A Quantitative Analysis in Terms of Four-Orbital-Model Parameters. *J. Phys. Chem.* **1985**, *89*, 4733–4739.
- (88) Mårtensson, J. Calculation of the Förster Orientation Factor for Donor-Acceptor Systems with One Chromophore of Threefold or Higher Symmetry: Zinc Porphyrin. *Chem. Phys. Lett.* **1994**, 229, 449–456.